


RESEARCH ARTICLE

Application of compression optical coherence elastography for characterization of human pericardium: A pilot study

Vladimir Y. Zaitsev¹  | Alexander A. Sovetsky¹ | Alexander L. Matveyev¹ | Lev A. Matveev¹ | Dmitry Shabanov¹ | Victoria Y. Salamatova^{2,3} | Pavel A. Karavaikin² | Yuri V. Vassilevski^{2,3,4}

¹Institute of Applied Physics, Russian Academy of Sciences, Nizhny Novgorod, Russia

²Sechenov University, Moscow, Russia

³Sirius University of Science and Technology, Sochi, Russia

⁴Marchuk Institute of Numerical Mathematics, Russian Academy of Sciences, Moscow, Russia

Correspondence

Vladimir Y. Zaitsev, Institute of Applied Physics, Russian Academy of Sciences, Nizhny Novgorod, Russia.
Email: vyuzai@ipfran.ru

Funding information

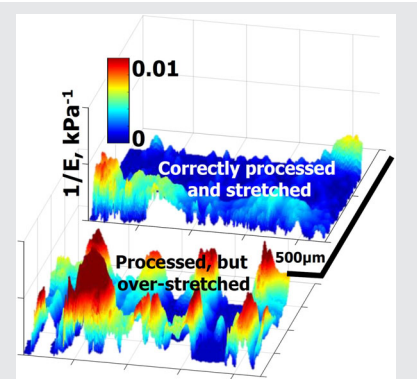
Russian Science Foundation, Grant/Award Numbers: 21-71-30023, 22-12-00295

Abstract

The recent impressive progress in Compression Optical Coherence Elastography (C-OCE) demonstrated diverse biomedical applications, comprising ophthalmology, oncology, etc. High resolution of C-OCE enables spatially resolved characterization of elasticity of rather thin (thickness < 1 mm) samples, which previously was impossible. Besides Young's modulus, C-OCE enables obtaining of nonlinear stress-strain dependences for various tissues. Here, we report the first application of C-OCE to nondestructively characterize biomechanics of human pericardium, for which data of conventional tensile tests are very limited and controversial. C-OCE revealed pronounced differences among differently prepared pericardium samples. Ample understanding of the influence of chemo-mechanical treatment on pericardium biomechanics is very important because of rapidly growing usage of own patients' pericardium for replacement of aortic valve leaflets in cardio-surgery. The figure demonstrates differences in the tangent Young's modulus after glutaraldehyde-induced cross-linking for two pericardium samples. One sample was over-stretched during the preparation, which caused some damage to the tissue.

KEYWORDS

compression elastography, human pericardium, OCE, optical coherence elastography, tissue biomechanics



1 | INTRODUCTION

In this study for the first time, we applied quantitative compression optical coherence elastography (C-OCE) to characterize samples of human pericardium. Pericardium represents a thin membrane that covers the heart. Pericardium is typically ~200 to 400 μm thick. The biomechanical

properties of pericardium are of interest because it is widely used as a material for a range of cardiac procedure [1]. Traditionally, bioprosthetic heart valves are composed of bovine pericardium. The past decade has seen the rapid spread of utilizing autologous human pericardium for aortic valve replacement owing to its biocompatibility and resistance to structural valve deterioration. However, the first

attempt to replace the aortic valve with native autologous pericardium failed [2] because of its poor biomechanical properties, low elastic modulus and rapid calcification. The use of autologous pericardium experienced a renaissance since conditioning of biological tissues with glutaraldehyde solution was introduced [3] and this method was adapted for intraoperative treatment of autologous pericardium [4]. Usually, the pericardial flap is prestrained (stretched) while treating.

Currently, the most appropriate technique of aortic valve autologous pericardial replacement is “Aortic Valve Neocuspidization” (AVNeo) developed by Ozaki et al. [5]. In the course of AVNeo procedure the three neo-leaflets are cut out from an autologous pericardial flap; the size of the leaflets which depends on the intercommissural distance of each native leaflet. Subsequently, the neo-leaflets are sewn to the aortic annulus. Figure 1 gives a representation about the form of the neo-valve and procedures of cutting the leaflets. A characteristic feature of Ozaki neo-leaflets is their larger area in comparison with the native aortic leaflets. Hence, the neo-leaflets provide a larger coaptation zone (see Figure 1B), which is beneficial for avoiding blood backflow (regurgitation). Nevertheless, large area of the neo-leaflets may cause blood clot formation on their surface [6].

Simulation-based neo-leaflet design makes it possible to avoid thrombosis and other adverse events and determine the patient-specific appropriate size and shape of the aortic valve neo-leaflets [7–10]. The correct mechanical properties of neo-leaflet tissues, such as chemically treated autologous pericardium, are an essential part of the recently developed mathematical modeling approaches based on computer simulations [11, 12]. These numerical methods are able to simulate heart valve functioning taking into account the mechanical properties of the leaflets, their

geometry, and their interaction with blood flow. Consequently, sufficiently ample understanding of the elastic properties of pericardium, including the difference between the native state and treated one, are of high interest. Conventionally the elastic properties of such thin membrane-like tissues have been studied using tensile tests. Such tests are essentially destructive by their nature, for example, uniaxial tests usually require preparation of special “dog-bone” shaped samples from an excised sufficiently large piece of the tissue. The tests themselves are rather laborious and time consuming. Usually they imply simultaneous acquisition of several different parameters (e.g., the applied force together with axial geometrical size and sometimes also lateral sizes).

The research to date has tended to focus on the mechanical behavior of heterologous (animal) pericardium rather than human one. However, their properties may significantly differ [13]. Furthermore, results of such studies are somewhat controversial. This can be illustrated briefly by contradicting evidence on the influence of chemical treatment on the mechanical properties of pericardium. Some research showed that pericardium becomes stiffer [14], whereas other ones demonstrated that it becomes softer [15, 16]. This disagreement is probably related to the different experimental techniques and protocols, since there are no standards for soft tissue experimental investigations, although the tensile tests are mostly used in these studies.

In the recent decades, several types of elastographic techniques have been developed to enable quantitative characterization of elastic properties of biological tissues [17, 18], most of those techniques being based on ultrasonic imaging. They have insufficient spatial resolution to characterize elasticity of thin tissue samples such as pericardium with a typical thickness of ~ 0.5 mm and

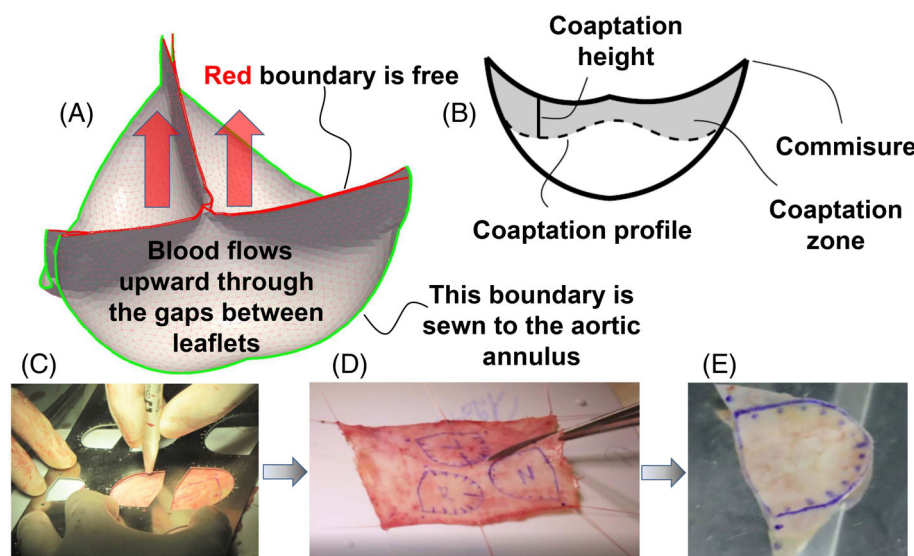


FIGURE 1 Schematic diagram of the three-leaflet valve (A) and one of the leaflets (B). Photos (C), (D) and (E) demonstrate stages of the valve preparation. Panel (A) shows the valve in the closed state and the arrows indicate the blood flow direction when the valve is open (when there appear gaps between contacting surfaces of the leaflets). The characteristic diameter of the central leaflet area shown in (E) is 15–30 mm depending on the patient

even less. Alternative methods for characterization of elasticity on a microscopic level (e.g., atomic-force microscopy techniques) on the contrary have too high resolution and are better suitable to characterize the elasticity of individual cells and even their constituents with a sub-cellular resolution.

Until recently there were no elastographic methods to fill the gap between the macroscopic and microscopic elastographic techniques. However, a significant progress has been demonstrated in this direction during the last 5–7 years in the development of quantitative elastographic methods termed optical coherence elastography (OCE) that uses optical coherence tomography as the basic imaging technique. Some of such methods use OCT to measure shear- or surface-wave velocities [19]. Another group of OCE methods utilizes the compression principle initially formulated for ultrasound [20] and then proposed for transferring to OCT by Schmitt [21] in 1998. Initially paper [21] suggested that motion of scatterers in the compressed tissue should be estimated using correlation tracking. However, the breakthrough in advancing compression OCE (C-OCE) to practical demonstrations was achieved using the phase-sensitive principles [22, 23] in combination with utilization of reference silicone layers as optical stress sensors [24, 25].

In this study, we report the results of the first application of OCE for the characterization of the elastic properties of human pericardium. This investigation was approved by the local ethical committee and conducted in accordance with the principles of the Declaration of Helsinki. Informed consent from the patient was obtained.

2 | MATERIALS AND METHODS

2.1 | Basic OCT setup

The used custom-made spectral-domain OCT setup with a central wavelength of 1300 nm and a spectral width of about 90 nm made it possible to obtain 3D OCT scans, as well as elastographic B-scans. A similar OCT setup was previously applied to visualize fine details of spatial distribution of strains and changes in elasticity (produced by heating with an IR laser) in corneal tissue samples [26, 27]. The thickness of corneal samples was comparable with that of pericardium samples used in the present study, which made it possible to use basically similar OCT scanner as in studies [26, 27]. The rate of obtaining spectral fringes was 80 kHz and the rate of acquiring B-scans 1024×512 pixels in size was 20 Hz (the B-scan size corresponded to 4 mm laterally and 2 mm in depth in air). The lateral resolution of structural OCT scans

determined by the radius of the optical beam was $\sim 15 \mu\text{m}$ and axial resolution determined by the coherence length was about 8 μm in air.

2.2 | Compression OCT elastography

The principle of phase-resolved C-OCE utilized in this study is shown in Figure 2, where Figure 2A schematically shows the experimental configuration. The reference silicone layer serves from quantification of the Young's modulus of the studied tissue by comparing the estimated axial phase gradients in the tissue and silicone. Figure 2B demonstrates a real example of interframe phase variations produced by the compression applied by the OCT probe to the sandwich structure "silicone-pericardium." Figure 2C shows an example of interframe strains estimated by calculating axial gradient of interframe phase variations using the vector method described in papers [28, 29].

A photo of the experimental procedure is shown in Figure 3, where a pericardium sample compressed by the OCT probe through the layer of reference silicone is shown. To prevent variation in the tissue properties due to drying we ensured that the sample was wet using the physiological saline solution. It is also important to emphasize that due to utilization of the precalibrated silicone layer no auxiliary means for estimating the applied stress were required. Furthermore, as discussed in detail in ref. [30, 31] conventional means such as force cells enable estimation of only mean stress, whereas in measurement with real tissues the stress may pronouncedly vary even within a single OCT scan because of non-ideally planar geometry of samples, their internal mechanical heterogeneity and nonlinearity. Therefore, the possibility to control the applied stress with spatial resolution using the silicone layers as distributed stress sensors is very important for correct quantification of tissue elasticity [30]. In particular, the technique described in [30] allows one to reassemble the initially obtained series of OCE scans of the deformed tissue and synthesize OCE scans with the same chosen stress level over the entire "stress-standardized" scan.

The next point of key importance for the reported study is the developed method allowing one to evaluate not only the Young's modulus for very small strains (below 1%, which is typical for OCT-based elastography), but also to obtain full stress–strain curves in a fairly broad strain range on the order of $\sim 10\%$ and even greater. The principle of this method is based on the experimentally proved very high elastic linearity of silicone. This highly-linear elastic behavior of silicones can be instructively demonstrated using a kind of

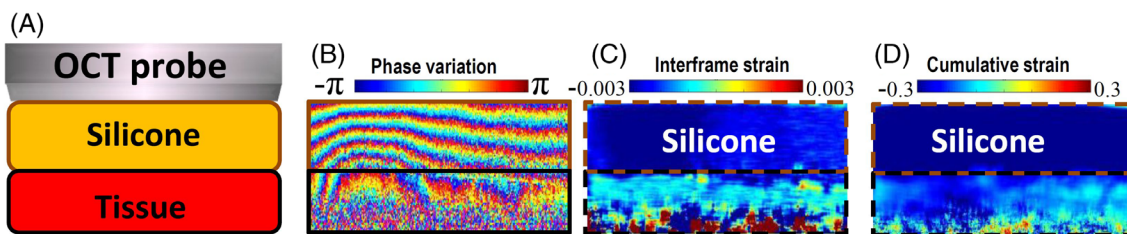


FIGURE 2 Principle of the used C-OCE method. (A) Is the schematically shown experimental configuration; (B) is an example of interframe phase variations; (C) is the map of interframe strains proportional to the axial gradients of interframe phase variations, and (D) is the distribution of cumulative strain found by summation of about 150 interframe strains

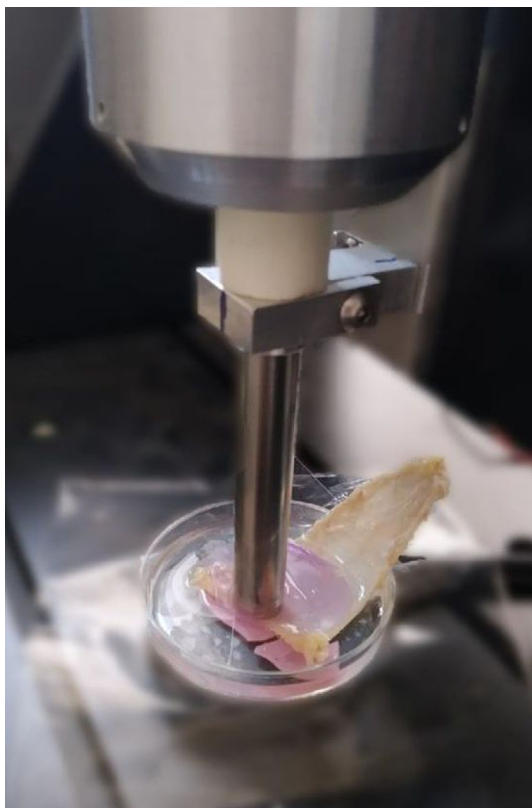


FIGURE 3 Experimental configuration for characterization of pericardium samples using the compression elastography principle

self-calibration test, the essence of which is illustrated in Figure 4A,B. Figure 4A shows an OCT image of sandwich structure composed of two layers of silicone with strongly contrasted Young's moduli (the ratio of the two moduli may be ~ 4 to 10). When compressed by the OCT probe the applied stress is the same for two layers. An incremental increase in stress $\Delta\sigma$ produces in silicone layers A and B incremental strains $\Delta\epsilon^{(A)}E_A = \Delta\sigma$ and $\Delta\epsilon^{(B)}E_B = \Delta\sigma$, the ratio of these incremental strains is evidently $\Delta\epsilon^{(A)}/\Delta\epsilon^{(B)} = E_B/E_A$, so that the strain in the softer silicone is significantly greater than that in the stiffer sample. The cumulative strains defined as

$$\epsilon^{(A, B)} = \sum_i \Delta\epsilon_i^{(A, B)} \quad (1)$$

should demonstrate invariable ratio $\epsilon^{(A)}/\epsilon^{(B)}$ in a broad strain range (up to tens percent) only if the elastic moduli $E_{A,B}$ remain invariable, independent of the current cumulative strains. Notice that the alternative definition of cumulative strain through the total variation in thickness of the visualized layers may lead to appreciable artefactual nonlinearity of geometrical origin for strains >0.15 to 0.2 (see reference [32]).

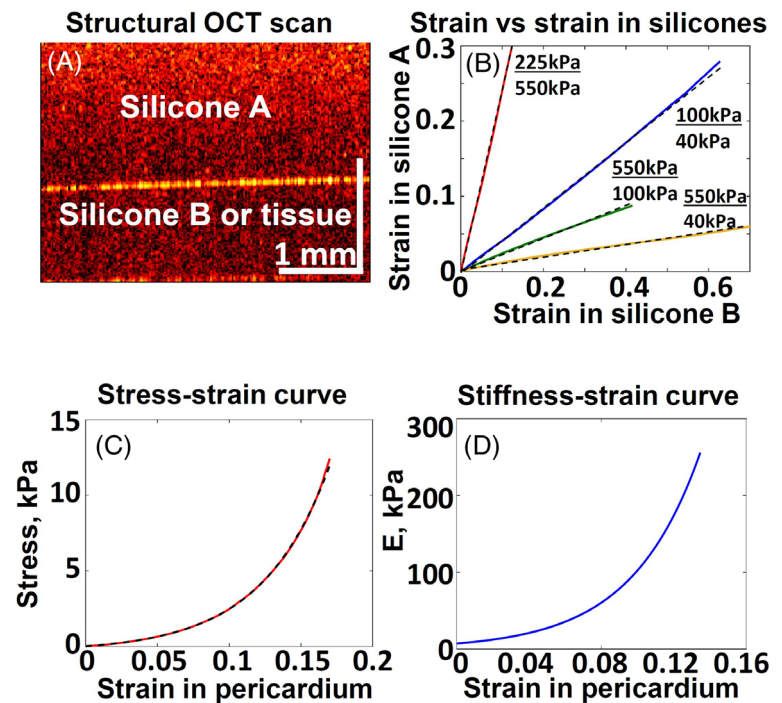
In other words, the slope of the dependence of cumulative strain $\epsilon^{(A)}$ on the other strains $\epsilon^{(B)}$ should remain constant only for two highly linear materials. Examples of such experimentally obtained plots of cumulative strains for highly contrasted in stiffness silicones, are presented in Figure 4B.

Figure 4B clearly demonstrates that indeed the elastic behavior of silicones is highly linear and very different from the behavior of pericardium. The corresponding examples for pericardium are shown in Figure 4C,D, for obtaining which a pericardium sample was used instead of silicone B. The high linearity of silicone guarantees that cumulative strain in the reference silicone is linearly proportional to the applied stress. Therefore, if the Young's modulus of the reference silicone is known, the strain of this reference silicone can be used for quantification of the applied stress. Thus, by plotting cumulative strains in silicone against cumulative strain of the studied tissue one can obtain its stress-strain dependence $\sigma(\epsilon)$ (which may be pronouncedly nonlinear as in Figure 4C). The current (tangent) Young's modulus corresponds to the current slope of this dependence

$$E_{tg} = d\sigma/d\epsilon. \quad (2)$$

The current slope of the dependence $\sigma(\epsilon)$ can be found, for example, analytically as the derivative of an analytically defined fitting function for the experimentally

FIGURE 4 Elucidation of the procedures used for obtaining nonlinear stress–strain curves using measurements with highly linear silicone samples. (A) Is the structural OCT image of a sandwich structure consisting of the reference silicone layer and the second layer (which may be either another silicone or a real tissue); (B) shows examples of plots of cumulative strain in one silicone layer “A” as a function of cumulative strain in another silicone layer “B” with a highly contrasted Young’s modulus; (C) experimental example of nonlinear stress–strain dependence for a pericardium sample obtained using the reference silicone as an optical stress sensor (the dashed line shows the fitting curve); (D) dependence of the Young’s modulus on strain found by differentiation of the fitting curve in panel (C)



observed $\sigma(\varepsilon)$. In Figure 4C such a fitting function is shown by the dashed line. Figure 4D shows the fitting-function derivative (i.e., the tangent Young’s modulus E_{tg}) plotted as a function of cumulative strain $E = E_{tg}(\varepsilon)$. Also, using the stress–strain dependence $\sigma(\varepsilon)$, such as that in Figure 4C, the tangent (current) Young’s modulus can readily be re-plotted as a function of stress. Using the described method we will show in what follows that, depending on the chemo-mechanical treatment of pericardium samples, both linear and nonlinear elastic properties of pericardium demonstrate strong differences.

In the described experiments, we used a silicone layer with the Young’s modulus $E \approx 100$ kPa. Such a modulus value appeared to be rather convenient for studying human pericardium.

2.3 | Sample preparation

The studied samples of the human pericardium were obtained from patients in the course of surgical procedures of the aortic valve neocuspidization using the own patient’s pericardium for fabrication of valve leaflets. Usually the excised piece of pericardium is larger than the total area of the tissue required for cutting the leaflets as illustrated in Figure 1, so that the excess tissue was used in the below described experiments. For comparison, a piece of the tissue was intentionally left in the native state.

According to the widely used Ozaki protocol, the tissue processing comprises the chemical fixation in the

glutaraldehyde normally in combination with a moderate stretching of the tissue. The chemical processing with glutaraldehyde causes additional cross-linking in the collagenous matrix of pericardium, so that a priori some stiffening of the chemically processed tissue can be expected. To clarify the role of mechanical stretching we also studied the chemically processed pieces which were not subjected to stretching. They were compared with moderately stretched samples according to the standard protocol of valve prosthesis preparation, as well as chemically processed samples that were subjected to over-stretching. Figure 5 presents the 3D OCT images for the above-mentioned four types of pericardium samples.

3 | RESULTS

3.1 | Comparison of the Young’s modulus for differently prepared pericardium samples

First, it was found that the processing procedures very clearly affected the Young’s modulus of the samples. In such measurements one should bear in mind possible influence of the tissue nonlinearity on the observed Young’s modulus (see the discussion of Figure 4). Consequently, to exclude the nonlinearity-related ambiguity, the Young’s modulus of compared samples should be estimated under the same conditions. In the discussed case, the tangent Young’s was estimated for the same

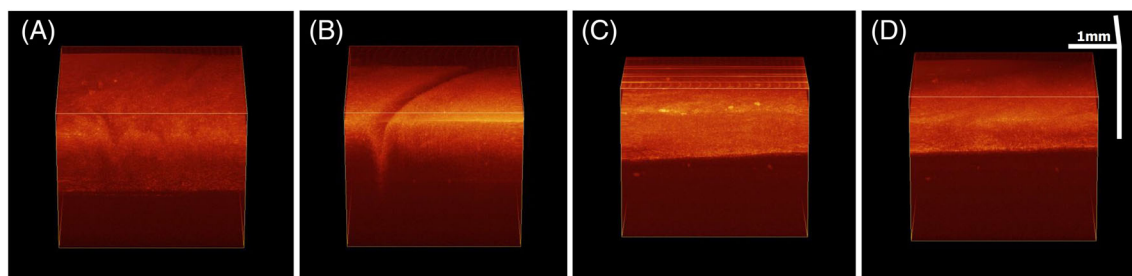


FIGURE 5 Obtained 3D images of the four types of the studied pericardium samples. (A) Is the sample in the native state; (B) is the chemically processed, but nonstretched sample; (C) is the chemically processed and stretched sample according to the standard protocol of pericardium preparation for fabrication of coronary-valve prostheses; (D) is the chemically processed, but to strongly stretched sample

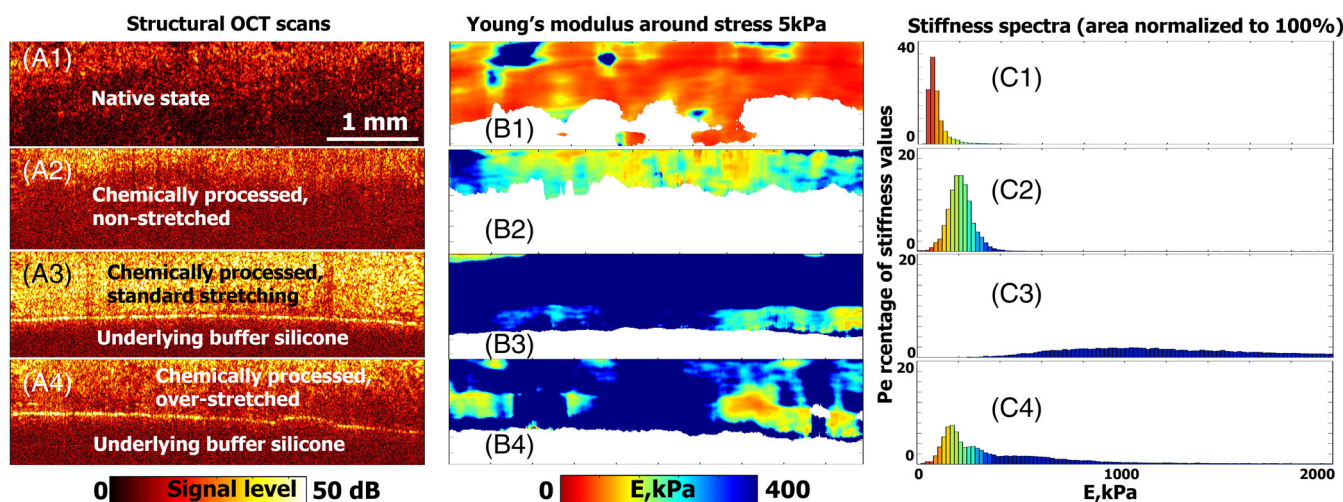


FIGURE 6 Result of comparative OCE-characterization of the four types of pericardium samples described in Section 2.3. Column (A) shows structural B-scans of the compared samples (the upper layer of the reference silicone is cropped and in panels (A-3) and (A-4) another buffer layer of silicone placed below the thinner pericardium samples is visible); column (B) shows the corresponding reconstructed maps of the Young's modulus obtained for the same stress level of 5 kPa using the reference silicone as an optical stress sensor (the white color corresponds to the areas of too low signal insufficient for reliable estimation of strain); column (C) shows the histograms of the Young's modulus distribution over the entire areas of the reconstructed stiffness maps shown in column (B), the total areas of histogram bins are normalized to unity. The histograms in column (C) clearly show how the characteristic stiffness for differently prepared samples depends on the preparation procedures; the most stiff is the chemically treated and moderately stretched pericardium (see row 3). Here, the overlying reference silicone is eliminated to clearer show the results for the pericardium thickness

stress level of 5 kPa. The results are summarized in Figure 6.

It is clear that pericardium in the native state demonstrates the lowest values of the Young's modulus localized in the vicinity of $E \sim 80\text{--}120$ kPa, whereas the three other samples demonstrate significantly higher stiffness. The difference in the Young's modulus among the compared samples in Figure 6 is demonstrated in two different forms: Young's modulus maps in column (B) and histograms in column (C), in which the proportions among various stiffness values over the stiffness maps presented in column (B) in Figure 6. The areas of the histograms are normalized to unity. It is clear that in comparison with the native state the chemically processed with

glutaraldehyde pericardium demonstrates higher Young's modulus. For the nonstretched sample, this increase is moderate with a fairly broad distribution of the Young's modulus centered around ~ 200 kPa (see panel [C-2] in Figure 6). However, the most stiff is the sample prepared according to the standard protocol (i.e., chemically processed and stretched pericardium), for which the spatial distribution of the Young's modulus is fairly uniform (see panel [B-2] in Figure 6), in which the stiffness values are almost everywhere above 300–400 kPa (see also the histogram in panel [C-2]).

Finally, for the over-stretched sample, evidently some portion of the internal links and collagen fibers in the tissue become broken, so that localized areas of soft tissue

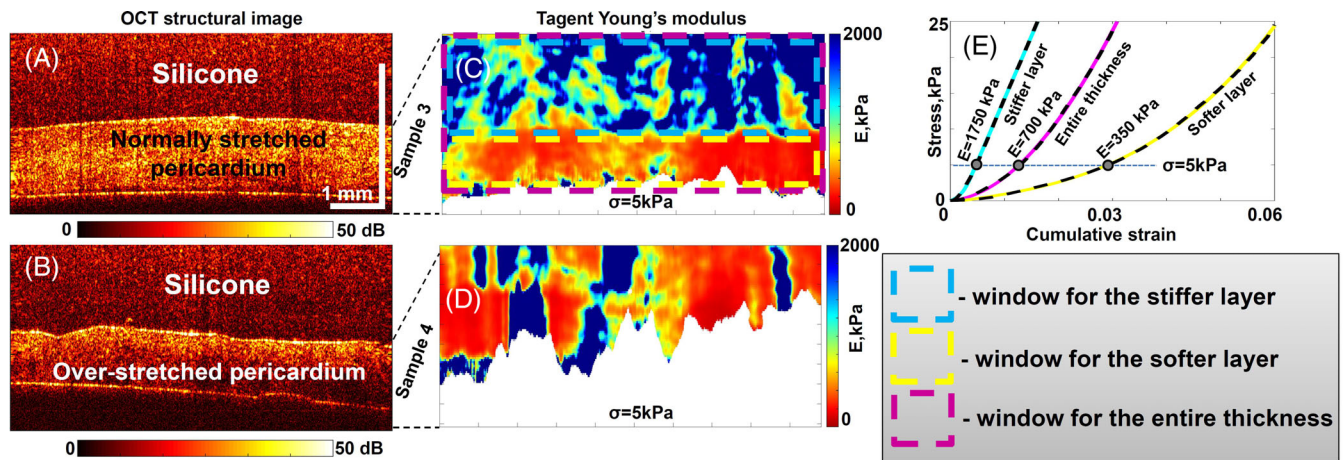


FIGURE 7 More detailed representation of OCE-examination results for the normally stretched and over-stretched pericardium samples. Panels (A) and (B) are structural images; (C) and (D) are the reconstructed maps of the tangent Young's modulus for 5 kPa stress showing pronounced layered inhomogeneity of the chemically treated and normally stretched sample; (E) shows the stress–strain curves for this sample found for each of the two layers and with averaging over the entire thickness (the horizontal dashed line shows 5 kPa stress level, for which the tangent Young's modulus was estimated)

(with E below 150–200 kPa) are seen in Figure 6 on the stiffness map (B-4) and the histogram (C-4) consistently demonstrates a significant portion of much lower Young's modulus values in comparison with the normally stretched sample.

We note that in the middle column in Figure 6, for all four elastograms the color coding range is the same and is chosen to clearer show the inhomogeneity of stiffness in the softer samples 1 and 2 (i.e., native and chemically treated, but unstretched sample). However, as is clear from the histograms of the stiffness values (column 3 in Figure 6), details of the spatial distributions in the much stiffer samples 3 (chemically treated and correctly stretched) and 4 (treated and over-stretched) are not sufficiently clear because of the color-coding saturation for stiffness values above 400 kPa. The next Figure 7 shows the elastograms for these two samples using a broader range of color coding (up to 2000 kPa similarly to the range in the histograms in Figure 6). In the structural images in Figure 7A,B, both upper reference silicone and underlying buffer silicone are intentionally left to clearer show that the chemically treated and stretched sample is much thinner than the native and unstretched ones and the entire sample thickness is seen very well. Elastograms in Figure 7C,D due to the 5 times broader range of color coding clearly reveal stiffness inhomogeneity of these samples, which was not well visible in Figure 6. It is noteworthy that stiffness distribution in Figure 7C for the chemically treated and normally stretched sample has a pronounced layered structure with a softer layer occupying almost 40% of the total thickness with stiffness localized in the range 400–500 kPa. The second layer is

characterized by 2–5 times higher stiffness. The resolution of OCE easily allows one to obtain the stress–strain curves not only averaged over the entire sample thickness, but also for the two layers separately even for $<400 \mu\text{m}$ thickness. Figure 7E shows three stress–strain curves with strongly differing slopes obtained for the upper stiffer layer (upper blue window), lower softer layer (yellow window) and the result of averaging over the entire thickness (wide magenta window).

This layered structure indicates that during functioning of a valve leaflet made of such tissue the mechanical load is mostly borne by the stiffer layer rather than the entire noticeably larger thickness. Also, during the leaflet bending, the neutral plane of zero straining is located within the main-load-bearing stiff layer and strains in the latter are noticeably smaller than expected for a uniform tissue with the same total thickness. In the softer, easier deformable layer, the strain is on the contrary somewhat larger.

In the overstretched sample, however, the layered structure disappears and the inhomogeneity is mostly in the lateral direction with intermittent stiffer and softer regions. The appearance of the latter evidently is explained by appearance of appreciable portions of damaged and weakened collagenous bundles because of overstretching.

Now we recall that the elastograms in Figures 6 and 7 demonstrate the maps of the tangent Young's modulus (i.e., the slope of stress–strain curves) for a particular stress level around 5 kPa. Examples of stress–strain curves in Figure 7 demonstrate that these curves exhibit pronounced nonlinearity, so that their slope essentially

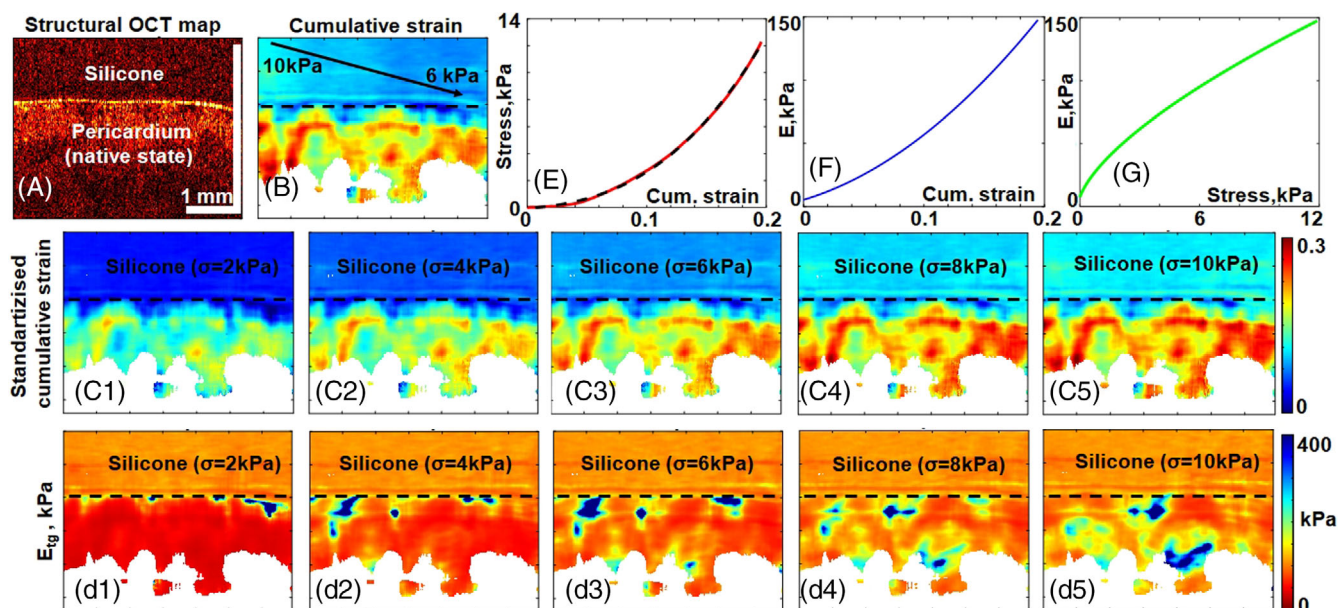


FIGURE 8 Demonstration of the dependence of the maps of cumulative strains and tangent Young's modulus on the applied stress taking as an example pericardium in the native state. Panel (A) is the structural scan; (B) is one of initially obtained maps of cumulative strain, for which the strain inhomogeneity in the reference silicone indicates pronounced inhomogeneity of stress applied to the pericardium (in this example, from 10 kPa in the left part of the scan (B) down to 6 kPa in its right part). Panels (C-1) through (C-5) are synthesized “standardized” maps of cumulative strains corresponding to various levels of uniform strain in the silicone, that is, uniform stress applied to the tissue; (D-1) through (D-5) are the maps of tangent Young's modulus corresponding to various levels of stress, panel (E) is the stress–strain dependence for the processing window covering the entire visualized area of pericardium (the dashed line shows the fitting curve); (F) is the derived dependence of the tangent Young's modulus E_{tg} on the tissue strain and (G) is E_{tg} replotted as a function of applied stress

depends on the chosen stress level. Another noteworthy issue is that even for a single scan, stress may appreciably vary along the lateral coordinate. This effect is very pronounced for mechanically strongly heterogeneous cancerous samples [30]. The pericardium samples are less heterogeneous but still may have appreciable thickness variations. For rather thin pericardium with a total thickness of 300–500 μm , even variations in thickness \sim tens of micrometers may already cause pronounced inhomogeneity of stress in the compressed sample. To deal with this inhomogeneity, we use the approach described in [30] based on synthesis of “standardized” elastograms with laterally uniform stress level of a pre-selected level. Such standardized images are made of the initial series of OCT scans obtained during compression of the sample. Figure 8 demonstrates utilization of this method of obtaining stress-standardized elastograms taking as an example the softest sample in the native state (that was shown in the upper row in Figure 6). Figure 8A,B shows the structural image and nonstandardized map of cumulative strains obtained at some intermediate loading of the sample. The level of cumulative strains in the reference silicone layer indicates that the axial stress has an appreciable lateral inhomogeneity (from \sim 8 kPa down to \sim 6 kPa). A series of stress-standardized elastograms of

the cumulative strains synthesized using the approach [30] from the initial series of elastograms is shown in the second row in Figure 8. In these elastograms, the stress is already laterally uniform. Note further, that the differential definition of the tangent Young's modulus can be approximated as $E_{tg} = \Delta\sigma/\Delta\varepsilon$. Thus, subtraction of such neighboring elastograms of cumulative strains in fact gives the maps of current tissue compliance, that is, quantity $\propto 1/E_{tg}$. The map of inverse compliance with proper normalization to the stress increment $\Delta\sigma$ gives the distribution of the tangent modulus itself, E_{tg} . Such distributions of E_{tg} for several stress levels are presented in the third row in Figure 8 and demonstrate that variations in the applied stress by a few kPa cause quite significant variations in E_{tg} . This method of mapping E_{tg} approximates the derivative $d\sigma/d\varepsilon$ by the finite-difference cord $\Delta\sigma/\Delta\varepsilon$ and does not assume a specific form of stress–strain dependences. These forms may noticeably differ even in closely located components of real heterogeneous tissues as demonstrated in Figure 7E for different sublayers of pericardium.

Figure 8E for the native-state pericardium also demonstrates its stress–strain curve. To eliminate small-scale variations caused by natural tissue heterogeneity, this curve is plotted with averaging over the entire visualized

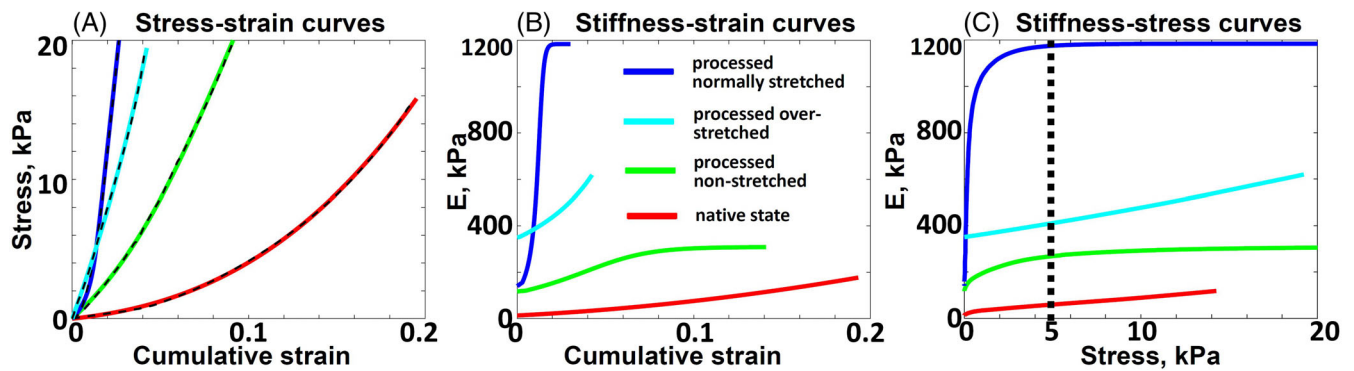


FIGURE 9 Comparison of the nonlinear dependences for the compared samples: Native, processed and nonstretched, processed and normally stretched, processed and over-stretched. Panel (A) shows the stress–strain curves, for which the dashed lines represent the fitting curves; (B) shows the Young’s modulus found via differentiation of the fitting curves from panel (A) $E_{tg} = d\sigma/de$ and plotted as a function of strain; (C) shows the similarly found Young’s modulus, but plotted as a function of stress. The vertical dashed line in (C) shows the stress value of 5 kPa, for which the stiffness maps and histograms in Figure 6 were plotted

tissue region. Certainly, the experimentally found stress–strain curves may be fitted by an analytical function (the dashed line in Figure 8E shows a fitting curve, for which a simple 3D-order polynomial is chosen). Then the approximating function may be differentiated to find tangent modulus E_{tg} that may be plotted as a function of either strain in the tissue or the applied stress. Figure 8F,G shows the so-obtained stiffness-strain and stiffness-stress laws corresponding to Figure 8E. The derived plots demonstrate that the tissue stiffness increases by an order of magnitude when the applied stress gradually increases towards ~ 10 to 12 kPa (whereas strain for the native sample reaches $\sim 20\%$). Just this nonlinearity is reflected in Figure 8C1–C5,D1–D5 in the spatially-resolved form.

Now, after elucidation of the developed procedures of obtaining stress–strain curves it is interesting to compare all four discussed samples not only in terms of a particular value of tangent Young’s modulus like in Figure 6, but also to consider the entire stress–strain curves and evolution of the tangent Young’s moduli for these differently prepared samples. The corresponding results are presented in Figure 9, in which panel (A) shows the stress–strain curves, for obtaining which the tissue strain is averaged over the entire visualized for each of the samples (see Figure 6). Figure 9B presents the tangent Young’s moduli for all four samples as a function of strain and 9C corresponds to dependences from Figure 9B replotted as a function of stress. In the experiments, for all four samples, we used similar maximal stress < 20 kPa controlled by observing the strain in the reference-silicone layer. However, because of the difference in stiffness among the samples the maximal strains for them significantly differ. An important observation is that pericardium in the native state at lower stress and strain is very soft (initially, modulus E is only 10–20 kPa),

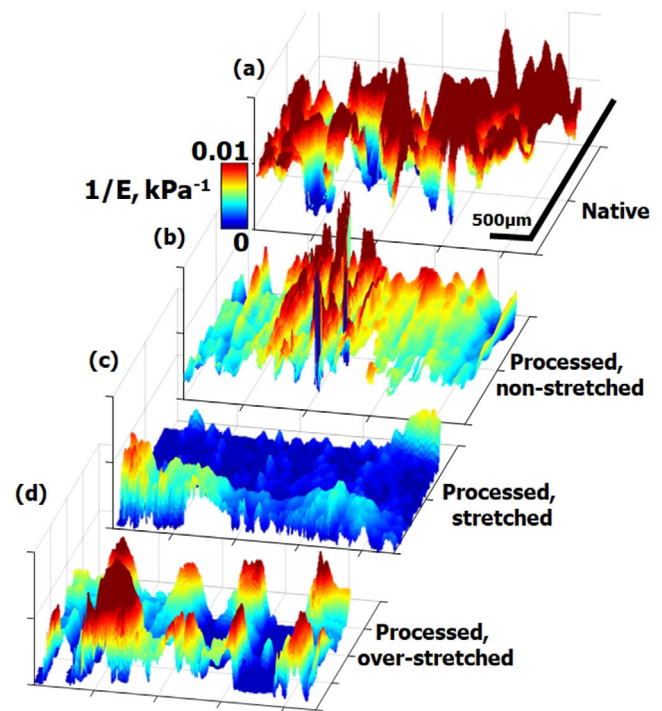


FIGURE 10 Illustration of spatial inhomogeneity of the tissue stiffness distribution. In these plots the 2D data similar to column (B) in Figure 6 are replotted in pseudo 3D-form for the inverse Young’s modulus $1/E$ rather than modulus E itself. Such a representation clearer shows the variability in the regions of lower stiffness values. Similarly to Figure 6 it is clear that the spatial distribution of stiffness is most homogeneous for the most stiff sample that was chemically processed and moderately stretched according to the standard Ozaki protocol

but increases up to almost 200 kPa for the maximal stress of 10 kPa.

It is also interesting that the chemically treated sample subjected to stretching according to the standard

procedures of aortic valve preparation initially is \sim twice softer than the overstretched sample, but then becomes the most stiff starting from moderate stress \sim 0.5 kPa and strain \sim 1% (see panels (B, C) in Figure 9). Another interesting observation is that for very small stress below 1 kPa and strains below 1%, the Young's moduli of the normally stretched and non-stretched samples nearly coincide, whereas the over-stretched sample is initially even stiffer than all other samples (see panel (B) in Figure 9).

It is essential to point out that the nonlinear dependences presented in Figure 9 were obtained with averaging over the total areas of OCE maps, excluding only noisy areas as shown in Figure 6. However, the same Figure 6 (column (B)) clearly demonstrates that the spatial distribution of the elastic properties of pericardium samples usually is rather spatially inhomogeneous with a characteristic inhomogeneity scale of the order of hundreds micrometers. The sample prepared according to the standard Ozaki protocol (chemically processed and normally stretched) looks the most homogeneous in Figure 6 showing the all four stiffness maps, although Figure 7 reveals regular layered structure of the normally stretched sample. To clearer characterize spatial inhomogeneity of the compared samples in another way, we represent the data from the central column (B) in Figure 6 as pseudo-3D maps in Figure 10, where the stiffness values are characterized by both color and height. Also, to clearer demonstrate the variability of both low and moderate stiffness values, in Figure 10 the inverse Young's modulus is plotted. The layered structure of the normally stretched sample is also recognizable in Figure 10C, as well as damaged spots in Figure 10D for the over-stretched sample.

In another form than in Figure 6 the plots in Figure 10 demonstrate that, except for the chemically treated and correctly stretched pericardium, the other three samples demonstrate pronounced spatial inhomogeneity of stiffness with a significant portion of regions with low stiffness. This pronounced spatial inhomogeneity of the studied tissue cannot be detected using conventional methods such as standard tensile tests.

Thus, the used C-OCE technique made it possible to perform a rather detailed characterization of variations in both linear and nonlinear elastic properties for differently prepared samples of human pericardium.

4 | DISCUSSION AND CONCLUSIONS

Similarly to the above-presented results numerous independent studies indicate that cross-linking caused by

chemical processing of collagenous tissues leads to a pronounced increase in the tissue stiffness. For example, various studies based on various types of OCT-elastography consistently indicate that cross-linking in corneal tissue caused by application of riboflavin and UV-irradiation leads to a pronounced increase in the cornea Young's modulus up to several times [33–35]. Similar stiffening in corneal tissue samples was also caused by formalin-induced cross-linking [31, 36]. The latter process is especially similar to the chemical treatment of pericardium with glutaraldehyde used in this study. In this context one can mention analogous conclusions that chemically-induced cross-linking caused stiffening of human pericardium were obtained in independent studies based on tensile tests [14]. For animal (usually bovine and porcine) pericardium, the effect of stiffening after chemically induced cross-linking is also confirmed (see, e.g. work [13]).

In contrast to such findings, however, in other studies [15, 16] of human pericardium based on tensile tests some reduction in the Young's modulus was mentioned. We should notice that for soft biological tissues there are no strict standard protocols of the tensile tests. Usually such uniaxial tests require “dog bone” samples. Qualitatively it is clear that the length of such samples should be sufficiently large to exclude the influence of boundary conditions, so that it is possible to consider that in the central part of the stretched sample the created stress is uniaxial and spatially uniform with a sufficiently high accuracy. For the conventional tensile tests, the strain is usually estimated via total variations in the sample length and the stress is calculated based on the measured tensile force and the estimated area of the sample cross section. In such measurements the above-mentioned assumptions about the absence of boundary effects and uniform uniaxial stress are not directly verified. Depending on the clamping method and sample geometry even for apparently “long” samples the boundary influence may be non-negligible and cause rather significant deviations of the estimated modulus from the actual Young's modulus of the tissue. In OCE the influence of boundary conditions may also distort the measurement results, however, the OCE ability to visualize strain distribution allows one to detect such distorting effects and undertake the corresponding measures to mitigate them [26].

An essential feature of elasticity of soft biological tissues is that their bulk modulus K is determined mostly by the compressibility of saturating water, for which $K \sim 2.25 \cdot 10^3$ MPa. This value is 10^3 – 10^5 times greater than the typical Young's modulus E of soft tissue. This statement is true even for cartilages with a fairly high Young's modulus E on the order of a few MPa. For other soft tissues, the ratio E/K is even much less. It is known from the theory of continua that, for tissues with

$K/E \gg 1$ their Poisson's ratio ν is very close to 0.5 (see, e.g., book [37]). If a material with $\nu \rightarrow 0.5$ is deformed by applying the uniaxial stress (no matter tensile or compressive), then the volume of the deformed tissue remains nearly invariable even if the form may strongly vary. Therefore, the assumption of incompressibility of soft biological tissues is widely used in interpretation of mechanical tests. At the same time there are known some studies, in which soft tissues were subjected to tensile stresses and demonstrated the apparent Poisson's ratios significantly (up to an order of magnitude) greater than 0.5. These findings were based on measurement of geometrical sizes (both axial and lateral) of stretched samples (see, e.g. [38] and refs. herein). These strongly elevated values of $\nu > 0.5$ indicate that during such tensile tests the tissue volume appreciably diminished instead of being nearly invariable. Usually it is difficult to find all the detail in descriptions of measurement procedures, which complicates the interpretation of unusual properties of tissues found in third-party measurements. One may hypothesize, for example, that for thin samples used in tensile tests the effects of sample drying through the open surface could cause the tissue shrinking and, consequently, the non-negligible diminishing of the tissue volume. In conventional tensile tests it is impossible to directly verify whether such effects as drying may be important, because strains in such tests are estimated by geometrical measurements of outer sizes without (or almost without) sufficient spatial resolution.

In contrast, the OCT-based technique described in this study readily enables a rather detailed spatially resolved mapping of strains, including strains in the tissue bulk. In previous tests of OCE techniques we found that for such collagenous tissue as cartilage, very pronounced water evaporation through the open surface is typical. Due to this natural drying the resultant shrinking-type strains may be rather strong: they easily reach several tens per cent during fairly short time intervals about several tens of seconds (see experimental examples of OCE observation of cartilage drying in paper [39]). Furthermore, the drying-induced shrinking may be so rapid that it may completely prevent observation of the opposite-sign strains that should be detected to verify the stability of circular-shape cartilaginous implants used in otolaryngology to treat trachea stenosis [40]. Such implants are prepared by bending thin cartilaginous plates combined with laser-induced relaxation of internal stresses [38]. Insufficiently relaxed stresses may cause undesirable and visually almost unnoticeable slow deformations. Sensitivity of OCE is quite sufficient to detect these slow strains, but drying-induced cartilage shrinking may strongly mask them [41]. To overcome this difficulty, special measures had to be used to prevent the tissue drying by applying thin protective plastic films [39].

The ability of OCE to enable spatially resolved strain visualization along with measurements of elastic parameters gives previously unavailable possibilities to readily detect possible masking effects, such as the influence of drying-induced shrinking [39] or apparent stiffening of the studied samples due to boundary conditions near areas of clamping or undesirable stiction [25]. Also the spatially-resolved mapping combined with obtaining nonlinear stress-strain curves is advantageous for finding optimal stress levels to enable enhanced contrast of various tissue components in terms of the tangent Young's modulus (e.g., for finding tumor boundaries [30, 42]) and even using in combination the Young's modulus and nonlinearity parameter [43].

Although tensile tests remain the most widely used and well established technique for mechanical characterization of membrane-like tissues, the unavoidable procedures of sample preparation for tensile tests are destructive. In this context, an important point is that even contact-mode OCE examinations described here are sufficiently delicate and biologically nondestructive for many applications. Concerning characterization of pericardium, the proposed technique of OCE-based estimation of the elastic properties, including obtaining of nonlinear stress-strain curves, may be a convenient, rapid and nondestructive alternative to the conventional tensile tests. The nondestructive nature is an important advantage of OCE. In particular, the pericardium samples discussed here may be studied directly in the very same areas from which the valve leaflets should be prepared.

Next, it should be noted that in the described form, compression OCE does not yet give information about the sample anisotropy, whereas tensile tests make it possible (although require either preparation of differently-oriented "dog bone" samples for uniaxial tests or organization of more complex loading like in biaxial tests). It may also be pointed out that, in principle, the ability of OCE to nondestructively characterize anisotropy has been demonstrated using another, wave-based realization of OCE [19, 44, 45]. In particular, for eye cornea it was demonstrated that measurements of surface wave velocities in various directions along the cornea surface may give a very instructive representation about anisotropy [44]. Also the possibility of noncontact excitation of surface waves is advantageous. However, simple and reliable relationship between the surface wave velocity and Young's modulus is available for Rayleigh waves propagating along the boundary of a half-space. For such thin membrane-like samples as pericardium, determining the excited wave type (other than Rayleigh wave) and, correspondingly, establishing of correct quantitative relationship between the Young's modulus and wave velocity is a more complex problem even for fairly homogeneous and

isotropic thin samples. For determining the wave-mode type, boundary conditions at both sample surfaces as well as thickness should be known [19, 46]. Thus, when contact mode is allowable, compression OCE may be more practical.

From the viewpoint of scales, the typical field of view of OCT scanners is \sim several millimeters independently of particular OCE realization. However, samples can be easily characterized on a scale of several centimeters by stitching several individual elastographic images and performing averaging when smaller scale variations in stiffness are not of interest.

Overall, the findings demonstrated in this study suggest that the C-OCE technique can be an efficient and biologically nondestructive tool to verify the modifications of the mechanical properties of pericardium depending on the type of its preparation. Simplicity and rapidity of the C-OCE technique facilitates examination of numerous samples to obtain statistically significant conclusions about the elastic properties of treated pericardium obtained from various patients and treated in different ways. This is a pivotal issue for the mathematical modeling and optimization of AVNeo procedures.

Certainly, in a broader sense the described technique can also be used for studying biomechanics of other tissues with similar membrane-like structure, such as intestine walls, as well as various samples fabricated by rapidly developing methods of tissue engineering.

ACKNOWLEDGMENTS

The reported studies were supported by the Russian Science Foundation (RSF), namely, the development of OCE-based technique and examination of the tissue samples were supported by the RSF grant 22-12-00295; the preparation of human pericardium samples in different states and analysis of the experimental results were performed under the support of grant No. 21-71-30023.

CONFLICT OF INTEREST

The authors have no conflict of interests to declare.

DATA AVAILABILITY STATEMENT

The data that support the findings of this study are available from the corresponding author upon reasonable request.

ORCID

Vladimir Y. Zaitsev  <https://orcid.org/0000-0002-2122-2943>

REFERENCES

- [1] A. De Martino, A. D. Milano, U. Bortolotti, *Thorac. Cardiovasc. Surg.* **2021**, 69, 83.
- [2] V. O. Björk, G. Hultquist, *J. Thorac. Cardiovasc. Surg.* **1964**, 47, 693.
- [3] A. Carpentier, G. Lemaigre, L. Robert, S. Carpentier, C. Dubost, F. Gerbode, *J. Thorac. Cardiovasc. Surg.* **1969**, 58, 467.
- [4] J. W. Love, J. H. Calvin, R. F. Phelan, C. S. Love, in *Biol. Bioprosthetic Valves. Proceeding Third Int. Symp. Card. Bioprotheses* (Eds: E. Bodnar, M. H. Yacoub), Yorke Medical Books, New York **1986**, p. 691.
- [5] S. Ozaki, I. Kawase, H. Yamashita, S. Uchida, Y. Nozawa, T. Matsuyama, M. Takatoh, S. Hagiwara, *Interact. Cardiovasc. Thorac. Surg.* **2011**, 12, 550.
- [6] H. Hayama, M. Suzuki, G. Hashimoto, K. Makino, Y. Isekame, H. Yamashita, T. Ono, R. Iijima, H. Hara, M. Moroi, *J. Am. Soc. Echocardiogr.* **2018**, 31, B62.
- [7] K. H. Lim, J. Candra, J. H. Yeo, C. M. G. Duran, *J. Heart Valve Dis.* **2004**, 13, 792.
- [8] P. E. Hammer, P. C. Chen, P. J. del Nido, R. D. Howe, *J. Biomech.* **2012**, 45, 1199.
- [9] K. Li, W. Sun, *Int. J. Numer. Methods Biomed. Eng.* **2017**, 33, e02814.
- [10] S. Travaglino, K. Murdock, A. Tran, C. Martin, L. Liang, Y. Wang, W. Sun, *J. Biomech. Eng.* **2020**, 142, 011007.
- [11] V. Y. Salamatova, A. A. Liogky, P. A. Karavaikin, A. A. Danilov, P. Y. Kopylov, G. V. Kopytov, O. N. Kosukhin, R. A. Pryamonosov, A. A. Shipilov, A. S. Yurova, Y. V. Vassilevski, *Russ. J. Numer. Anal. Math. Model.* **2019**, 34, 277.
- [12] A. Liogky, P. Karavaikin, V. Salamatova, *Mathematics* **2021**, 9, 2193.
- [13] P. Aguiari, M. Fiorese, L. Iop, G. Gerosa, A. Bagno, *Interact. Cardiovasc. Thorac. Surg.* **2016**, 22, 72.
- [14] V. Ozolins, I. Ozolanta, L. Smits, A. Lacs, V. Kasyanov, *14th Nordic-Baltic Conference on Biomedical Engineering and Medical Physics*, Springer, Berlin, Heidelberg **2008**, p. 143.
- [15] T. Zigras, *Biomechanics of Human Pericardium: A Comparative Study of Fresh and Fixed Tissue*, McGill University, Montreal, Canada **2007**. Master Thesis.
- [16] D. Tremblay, T. Zigras, R. Cartier, L. Leduc, J. Butany, R. Mongrain, R. L. Leask, *Ann. Thorac. Surg.* **2009**, 88, 1484.
- [17] K. J. Parker, M. M. Doyley, D. J. Rubens, *Phys. Med. Biol.* **2010**, 56, R1.
- [18] J. Ormachea, K. J. Parker, *Phys. Med. Biol.* **2020**, 65, 24TR06. <https://doi.org/10.1088/1361-6560/abca00>
- [19] M. Singh, F. Zvietcovich, K. V. Larin, *J. Opt. Soc. Am. A* **2022**, 39, 418.
- [20] J. Ophir, I. Cespedes, H. Ponnekanti, Y. Yazdi, X. Li, *Ultrason. Imaging* **1991**, 13, 111.
- [21] J. M. Schmitt, *Opt. Express* **1998**, 3, 199.
- [22] B. F. Kennedy, S. H. Koh, R. T. A. McLaughlin, K. M. Kennedy, P. R. T. Munro, D. D. Sampson, *Biomed. Opt. Express* **2012**, 3, 1865.
- [23] V. Y. Zaitsev, A. L. Matveyev, L. A. Matveev, A. A. Sovetsky, M. S. Hepburn, A. Mowla, B. F. Kennedy, *J. Biophotonics* **2021**, 14, e202000257.
- [24] K. M. Kennedy, L. Chin, R. A. McLaughlin, B. Latham, C. M. Saunders, D. D. Sampson, B. F. Kennedy, *Sci. Rep.* **2015**, 5, 1.
- [25] V. Y. Zaitsev, A. L. Matveyev, L. A. Matveev, E. V. Gubarkova, A. A. Sovetsky, M. A. Sirotkina, G. V. Gelikonov, E. V. Zagaynova, N. D. Gladkova, A. Vitkin, *J. Innov. Opt. Health Sci.* **2017**, 10, 1742006.

- [26] V. Y. Zaitsev, A. L. Matveyev, L. A. Matveev, G. V. Gelikonov, O. I. Baum, A. I. Omelchenko, D. V. Shabanov, A. A. Sovetsky, A. V. Yuzhakov, A. A. Fedorov, V. I. Siplivy, A. V. Bolshunov, E. N. Sobol, *J. Biophotonics* **2019**, *12*, e201800250.
- [27] O. I. Baum, V. Y. Zaitsev, A. V. Yuzhakov, A. P. Sviridov, M. L. Novikova, A. L. Matveyev, L. A. Matveev, A. A. Sovetsky, E. N. Sobol, *J. Biophotonics* **2020**, *13*, e201900199.
- [28] V. Y. Zaitsev, A. L. Matveyev, L. A. Matveev, G. V. Gelikonov, A. A. Sovetsky, A. Vitkin, *J. Biomed. Opt.* **2016**, *21*, 116005.
- [29] A. L. Matveyev, L. A. Matveev, A. A. Sovetsky, G. V. Gelikonov, A. A. Moiseev, V. Y. Zaitsev, *Laser Phys. Lett.* **2018**, *15*, 65603.
- [30] A. A. Sovetsky, A. L. Matveyev, L. A. Matveev, E. V. Gubarkova, A. A. Plekhanov, M. A. Sirotkina, N. D. Gladkova, V. Y. Zaitsev, *Laser Phys. Lett.* **2020**, *17*, 065601.
- [31] A. A. Sovetsky, A. L. Matveyev, L. A. Matveev, D. V. Shabanov, V. Y. Zaitsev, *Laser Phys. Lett.* **2018**, *15*, 085602.
- [32] A. A. Sovetsky, A. L. Matveyev, L. A. Matveev, G. V. Gelikonov, V. Y. Zaitsev, *J. Biomed. Photonics Eng.* **2022**, *8*, 1.
- [33] M. A. Kirby, I. Pelivanov, S. Song, Ł. Ambrozinski, S. J. Yoon, L. Gao, D. Li, T. T. Shen, R. K. Wang, M. O'Donnell, *J. Biomed. Opt.* **2017**, *22*, 1.
- [34] M. Singh, A. Nair, S. R. Aglyamov, K. V. Larin, *Photonics* **2021**, *8*, 111.
- [35] S. Kling, *J. R. Soc. Interface* **2020**, *17*, 20190786.
- [36] Y. Qu, T. Ma, Y. He, J. Zhu, C. Dai, M. Yu, S. Huang, F. Lu, K. K. Shung, Q. Zhou, Z. Chen, *IEEE J. Sel. Top. Quantum Electron.* **2016**, *22*, 288.
- [37] L. D. Landau, E. M. Lifshitz, *Theory of Elasticity*, Butterworth-Heinemann, Oxford **1986**.
- [38] R. C. Picu, S. Deogekar, M. R. Islam, *J. Biomech. Eng.* **2018**, *140*, 0210021.
- [39] V. Y. Zaitsev, L. A. Matveev, A. L. Matveyev, A. A. Sovetsky, D. V. Shabanov, S. Y. Ksenofontov, G. V. Gelikonov, O. I. Baum, A. I. Omelchenko, A. V. Yuzhakov, E. N. Sobol, *Laser Phys. Lett.* **2019**, *16*, 065601.
- [40] O. I. Baum, Y. M. Alexandrovskaya, V. M. Svistushkin, S. V. Starostina, E. N. Sobol, *Laser Phys. Lett.* **2019**, *16*, 035603.
- [41] Y. M. Alexandrovskaya, O. I. Baum, A. A. Sovetsky, A. L. Matveyev, L. A. Matveev, E. N. Sobol, V. Y. Zaitsev, *Laser Phys. Lett.* **2020**, *17*, 085603.
- [42] A. A. Plekhanov, M. A. Sirotkina, A. A. Sovetsky, E. V. Gubarkova, S. S. Kuznetsov, A. L. Matveyev, L. A. Matveev, E. V. Zagaynova, N. D. Gladkova, V. Y. Zaitsev, *Sci. Rep.* **2020**, *10*, 11781.
- [43] E. V. Gubarkova, A. A. Sovetsky, L. A. Matveev, A. L. Matveyev, D. A. Vorontsov, A. A. Plekhanov, S. S. Kuznetsov, S. V. Gamayunov, A. Y. Vorontsov, M. A. Sirotkina, N. D. Gladkova, V. Y. Zaitsev, *Materials* **2022**, *15*, 3308.
- [44] F. Zvietcovich, K. V. Larin, *Prog. Biomed. Eng.* **2022**, *4*, 012007.
- [45] F. Zvietcovich, M. Singh, Y. S. Ambekar, S. R. Aglyamov, M. D. Twa, K. V. Larin, *IEEE J. Sel. Top. Quantum Electron.* **2021**, *27*, 6800810.
- [46] J. J. Pitre, M. A. Kirby, D. S. Li, T. T. Shen, R. K. Wang, M. O'Donnell, I. Pelivanov, *Sci. Rep.* **2020**, *10*, 1.

How to cite this article: V. Y. Zaitsev, A. A. Sovetsky, A. L. Matveyev, L. A. Matveev, D. Shabanov, V. Y. Salamatova, P. A. Karavaikin, Y. V. Vassilevski, *J. Biophotonics* **2022**, e202200253. <https://doi.org/10.1002/jbio.202200253>